ACS APPLIED MATERIALS & INTERFACES

Research Article

www.acsami.org

Bulk Charge Carrier Transport in Push–Pull Type Organic Semiconductor

Supravat Karak, Feng Liu,† Thomas P. Russell,* and Volodimyr V. Duzhko*

Department of Polymer Science and Engineering, University of Massachusetts, Amherst, Massachusetts 01003, United States

Supporting Information

ABSTRACT: Operation of organic electronic and optoelectronic devices relies on charge transport properties of active layer materials. The magnitude of charge carrier mobility, a key efficiency metrics of charge transport properties, is determined by the chemical structure of molecular units and their crystallographic packing motifs, as well as strongly depends on the film fabrication approaches that produce films with different degrees of anisotropy and structural order. Probed by the time-of-flight and grazing incidence X-ray diffraction techniques, bulk charge carrier transport, molecular packing, and film morphology in different structural phases of push–pull type organic semiconductor, 7,7′-(4,4-bis(2-ethylhexyl)-4H-silolo[3,2-b:4,5-b′]dithiophene-2,6-diyl)-bis(6-fluoro-4-(5′-hexyl-[2,2′-bithiophen]-5yl)benzo[c][1,2,5] thiadiazole), one of the most efficient small-molecule photovoltaic materials to-date, are described herein. In the isotropic phase, the material is ambipolar with high mobilities for a fluid state. The electron and hole mobilities at the phase onset at 210.78 °C are 1.0×10^{-3} $cm^2/(V\ s)$ and 6.5×10^{-4} $cm^2/(V\ s)$, respectively. Analysis of the temperature and electric field dependences of the mobilities in the framework of Gaussian disorder formalism suggests larger energetic and positional disorder for electron transport sites. Below 210 °C, crystallization into a polycrystalline film with a triclinic unit cell symmetry and high degree of anisotropy leads to a 10-fold increase of hole mobility. The mobility is limited by the charge transfer along the direction of branched alkyl side chains. Below 90 °C, faster cooling rates produce even higher hole mobilities up to 2×10^{-2} $cm^2/(V\ s)$ at 25 °C because of the more isotropic orientations of crystalline domains. These properties facilitate in understanding efficient material performance in photovoltaic devices and will guide further development of materials and devices.

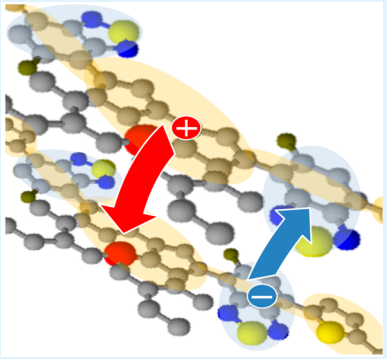

KEYWORDS: *push–pull organic semiconductor, ambipolar charge transport, mobility, time-of-flight, X-ray diffraction*

INTRODUCTION

Steady improvement of electronic and optoelectronic properties of organic semiconductors, favorable materials processability from solvents, and flexibility and light weight of devices promise to enable a variety of cost-effective applications. To follow the footsteps of organic light-emitting diodes en route to commercialization, organic field-effect transistors (OFETs), light-emitting transistors (OLET), and photovoltaic devices (OPVs) require further optimization.[1−3] Operation of these devices relies on charge transport properties of active layer materials, and in particular on charge carrier mobility. The magnitude of mobility is determined primarily by the chemical structure of constituent units (small molecules, oligomers, or polymers) and their solid-state packing motifs. Additionally, because typical device architectures are based on thin-film geometry, morphological characteristics of films such as anisotropy and alignment of the most efficient charge transport direction along the device operation direction, grain size, and degree of order depend on film fabrication, strongly affecting the magnitude of mobility too.

Push–pull type organic semiconductors which consist of electron-rich and electron-poor moieties with partial ground-state electron transfer have been dominating the field of organic photovoltaics for over a decade.[4−6] Recently, a new class of donor–acceptor copolymers with high charge carrier mobilities, on the order of 5–10 $cm^2/(V\ s)$ as measured in OFET configuration, i.e., field-effect mobilities, have been developed.[7,8] Despite remarkable progress in improving the overall power conversion efficiencies of OPVs because of utilization of push–pull type materials,[9,10] charge carrier mobilities, even in the best-performing photovoltaic materials, remain significantly lower. An insight into intrinsic charge transport properties of push–pull type semiconductors should lead to better understanding of the material functionality and device operation, and higher mobilities to further improvement of device performance.[11]

Development of highly efficient charge transport materials that are processed from organic solvents is typically related to the ability to create anisotropic films. In regioregular poly(3-hexylthiophene), efficient transport is ensured by the alignment of $\pi-\pi$ stacking direction in the lamella structures along the in-plane transport direction.[12] In push–pull type materials, the transport occurs primarily along the rigid backbone of the high-molecular-weight polymers, with occasional interbackbone

Received: August 18, 2014
Accepted: November 13, 2014
Published: November 13, 2014

charge transfer steps.[8,13] The rigidity of backbones arises from the intramolecular donor−acceptor interaction, i.e., electronic orbital hybridization, which keeps the backbones planar, preventing chain folding and extending the range of efficient intramolecular charge transport. Such transport mechanisms are possible due to a quasi-two-dimensional confinement of charge transport channels in OFET geometry to a few molecular layers at the interface with a gate dielectric.[14] On the contrary, photovoltaic devices rely on bulk charge carrier transport in orthogonal direction. Therefore, charge transport mechanisms that account for intermolecular charge transfer in three dimensions need be considered, unless the films are highly anisotropic. Time-of-flight (TOF) technique[15,16] allows studying the bulk charge transport normal to the electrode surface. The technique can yield charge carrier mobilities over a broad temperature and electric-field range and is not affected by the ambiguities that are associated with the temperature and electric field dependences of carrier density for intrinsic, photogenerated, or injected-from-the-electrodes charges. This, in turn, allows studying intrinsic charge carrier transport mechanisms in different structural phases, correlating the elementary intermolecular charge transfer processes with molecular chemical structure, packing motifs and film morphology, and identifying the processes that limit the magnitude of mobility.[17]

In this article, we describe correlated studies of bulk charge carrier transport and structural properties of push−pull type organic semiconductor, 7,7′-(4,4-bis(2-ethylhexyl)-4H-silolo-[3,2-b:4,5-b′]dithiophene-2,6-diyl)bis(6-fluoro-4-(5′-hexyl-[2,2′-bithiophen]-5yl)benzo[c][1,2,5] thiadiazole), (p-DTS-$(FBTTh_2)_2$), one of the most efficient small-molecule photovoltaic materials to date,[10,18] by the time-of-flight and grazing incidence X-ray diffraction (GIXD) techniques. We demonstrate the ambipolar nature of charge transport in the isotropic phase, discuss structural features that limit the magnitude of mobility in various structural phases at different temperatures, and describe an optimized film processing procedure that produces hole mobility of 2×10^{-2} $cm^2/(V\ s)$ at room temperature. These results facilitate in explaining efficient performance of p-DTS$(FBTTh_2)_2$ as a donor component in bulk heterojunction (BHJ) photovoltaic devices and will guide further development of materials and devices.

EXPERIMENTAL SECTION

Materials. The p-DTS$(FBTTh_2)_2$ (Figure 1) was purchased from 1-Material Inc.[19] The TOF samples were fabricated in a sandwich-type

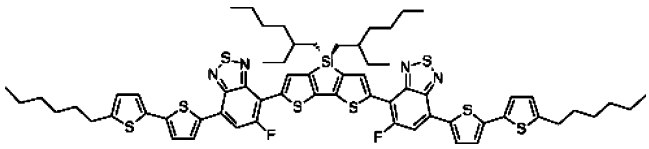

Figure 1. Molecular chemical structure of p-DTS$(FBTTh_2)_2$.

geometry using indium tin oxide (ITO) - coated rectangular glass substrates (20 Ω/□, Thin Film Devices Inc.). The substrates were cleaned in ultrasonic bath with detergent, deionized water (twice), acetone and isopropyl alcohol in 10 min steps. The empty 11 μm-thick (L) cells were constructed using silica beads that defined the cell thickness and were sealed with an electrically insulating epoxy (Omega, OB-200, expansion coefficient of 9.6×10^{-5} m/mK) on two opposite sides. The cells were then filled with p-DTS$(FBTTh_2)_2$ in its fluid state at 230 °C because of capillary forces and cooled to room temperature (~25 °C) at a constant rate using an HSC-2 heating stage and MK1000 controller (INSTEC). The differential scanning calorimetry (DSC) measurements (see Figure S1 in the Supporting Information) indicate that p-DTS$(FBTTh_2)_2$ melts at 210.78 °C on heating and crystallizes at 179.47 °C on cooling. Three different cooling rates of 1 °C/min ("slow cooling"), 10 °C/min and "rapid cooling" (discontinued source of heat, the fastest nonuniform cooling rate) were used to process TOF samples in this study. Additionally, the temperature-modulated DSC (see Figure S2 in the Supporting Information) shows a series of features in the range from ~65 to ~80 °C, indicating a subphase transition. All samples were prepared inside the glovebox (N_2, <1 ppm of O_2, <1 ppm of H_2O).

Experimental Techniques. TOF measurements were carried out using a custom-built apparatus. A third harmonic of pulsed Nd:YAG laser (Continuum Lasers, Surelite II, pulse duration 4−6 ns) at a wavelength of 355 nm was used for photoexcitation. The chosen wavelength resulted in a narrow sheet of photogenerated electrons and holes near the illuminated electrode. The photocurrent transients at different temperatures and electric fields were measured across a load resistor (R_L), chosen from a set of resistors from 50 Ω to 5 kΩ to ensure sufficient time resolution, by the Tektronix TDS 3052C oscilloscope. Positive or negative polarities of external bias voltage (V_0) with respect to the illuminated electrode determined if the photoexcited holes or electrons, respectively, moved through the film. A change of the slope in the photocurrent transients, which indicates the propagation of photoexcited charge carriers through the entire film, defined the transit time τ_{tr}. The τ_{tr} was determined from the intersection of tangent lines to the pre- and post-transit regions of the photocurrent transients in a double-logarithmic scale representation. The mobility was determined as $\mu = L^2/V_0\tau_{tr}$. The laser pulse intensity was kept low to avoid distortion of the electric field by the space charge.

Grazing incidence X-ray diffraction (GIXD) was done at beamline 7.3.3 of the Advanced Light Source, Lawrence Berkeley National Laboratory. In GIXD experiment, the samples were fabricated in the same way as they were for TOF measurements, except on polished silicon wafers as substrates. Samples were then loaded inside a helium chamber to eliminate air scattering and prevent material oxidation. 0.18° incidence angle was used in the experiment. Pilatus 1 M detector was used to record the diffraction signals and Nika software package was used to analyze the data. The X-ray energy was 10 keV. The sample-to-detector distance of ~30 cm was calibrated using AgB. In in situ experiment, a heating stage inside the helium chamber allowed controlling the temperature. During the heating cycle, an 8 min waiting time was used to achieve thermal equilibrium for each temperature point before measuring the diffraction pattern. In cooling experiments, the samples were naturally cooled under a helium flow, reproducing the "rapid cooling" procedure in TOF experiments, and diffraction patterns were measured continuously.

RESULTS AND DICSUSSION

Charge Carrier Transport. To study bulk charge carrier transport in different structural phases of p-DTS$(FBTTh_2)_2$, we measured the electron and hole mobilities at different temperatures and electric fields by the TOF technique. Shown in Figure 2 are the typical photocurrent transients measured at (a) 60, (b) 190, and (c) 250 °C for holes and (d) at 260 °C for electrons for different V_0. A common feature of the curves is the presence of three distinct time intervals: (i) immediately after the laser pulse when the photocurrent decays quickly due to thermal relaxation of photogenerated charge carriers, (ii) a plateau region which corresponds to the movement of photoexcited charge carriers through the film, and (iii) a rapid decay after τ_{tr} when the charges reach the opposite electrode. A clear shift of τ_{tr} to shorter times with increasing voltage indicates that the passage of photogenerated charges through the film is faster at larger electric field.

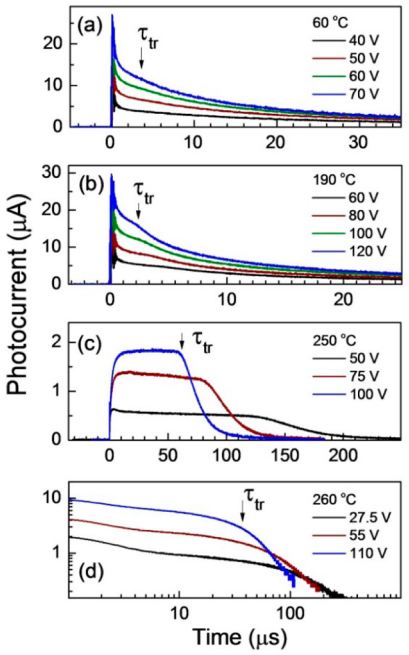

Figure 2. Typical photocurrent transients in different structural phases of p-DTS(FBTTh$_2$)$_2$ measured at (a) 60, (b) 190, and (c) 250 °C for holes and at (d) 260 °C for electrons. The arrows indicate τ_{tr} for the largest V_0 in each subfigure.

Interestingly, the photocurrent transients have distinct shapes at different temperatures. In ideal TOF experiment, the ultrathin sheet of photogenerated charge carriers creates a constant photocurrent after the laser pulse when the charges begin to drift from the illuminated electrode and until they reach the opposite electrode at τ_{tr}, at which point the photocurrent drops to zero, i.e., $I(t) = I_0$ for $t < \tau_{tr}$ and $I(t) = 0$ for $t > \tau_{tr}$. In practice, thermal relaxation of photogenerated charge carriers causes the initial decay of photocurrent immediately after the laser pulse. For a disordered organic semiconductor, the energy of an assembly of charge carriers generated randomly within a localized density of states described by a Gaussian distribution function of width σ, relaxes toward the tail states to attain a dynamic quasi-equilibrium with an average energy of $-\sigma^2/kT$ below the center of the density of states (see Scheme S1 in the Supporting Information).[20] The time to reach quasi-equilibrium given by $\tau_{rel}/\tau_0 = 10 \times \exp[-(1.07\sigma/kT)^2]$, where τ_0 is the dwell time of a carrier without disorder, is expected to be shorter for less disordered material and at higher temperatures. For hole transients above 210 °C (Figure 2c), the absence of the fast photocurrent decay indicates that the thermal relaxation occurs faster than the R_LC constant of the measurement circuit. At longer times before τ_{tr}, a nondispersive transport with the transients shape defined by only a Gaussian statistical broadening of the drifting charge sheet is observed as evidenced by a nearly constant photocurrent. The spread of the transit time due to energy dispersion and diffusion is given by $\Delta\tau_{tr}/\tau_{tr} = (2kT/eV_0)^{1/2}$,[20] which is on the order of 5×10^{-2} for the applied voltage of $V_0 = 50$ V in the given temperature range. On the other hand, the photocurrent transients for electrons above 210 °C (Figure 2d) are characterized by thermal relaxation of electrons on the time scale before 4 μs, followed by a more dispersive transport due to larger disorder of electron transport sites as evidenced by the slope of the photocurrent after thermal relaxation. At 190 °C (Figure 2b), the shape of the photocurrent for holes results from comparable thermal relaxation and transit times and, therefore, a well-developed plateau is not present. At 60 °C (Figure 2a), even more dispersive shape of the photocurrent transients results from the fact that the photogenerated charge carriers require more time to attain a dynamic quasi-equilibrium at lower temperature; larger disorder in this structural phase cannot be excluded too. The double logarithmic scale representation of the photocurrent transients (see Figure S3 in the Supporting Information) allows us to distinguish the pre- and post-transit time regions and to determine the values of τ_{tr} for holes at all measured temperatures however. On the other hand, despite a larger magnitude of photocurrent for electrons than for holes below 210 °C (not shown), no well-defined τ_{tr} was observed, making it impossible to determine electron mobility below 210 °C. The larger magnitude of photocurrent indicates that the short-range transport of electrons, on the time scale before the dynamic quasi-equilibrium is reached, is more efficient than that of holes. The electrons do not attain dynamic equilibrium on the time scale of transit time however.

Figure 3 shows the temperature dependence of hole mobility (Figure 3a) and electron mobility (Figure 3b) measured at an electric field of 2×10^4 V/cm on heating after p-DTS(FBTTh$_2$)$_2$ recrystallization from the isotropic phase at different cooling rates. In the isotropic phase above 210 °C, the material is ambipolar with electron and hole mobilities of 1×10^{-3} cm^2/(V s) and 6.5×10^{-4} cm^2/(V s), respectively, near the phase onset. Considering that the material is a fluid, these are very large mobilities for a disordered state.[21] An ambipolar transport with comparable electron and hole mobilities is often observed for push−pull type polymers with narrow bandgaps in OFET and OLET configurations.[3] In earlier generation of organic semiconductors that had symmetric HOMO and LUMO orbitals and, therefore, identical transfer integrals for electrons and holes, and comparable reorganization energies,[22] the unipolar behavior was attributed to such extrinsic factors as presence of oxygen and water, to chemical instability of materials and to charge trapping in the presence of these impurities.[23] The observation of ambipolar bulk charge carrier

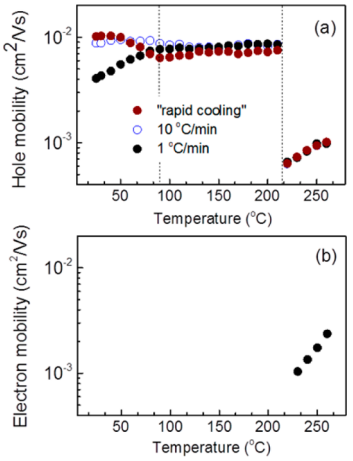

Figure 3. Temperature dependence of (a) hole mobility and (b) electron mobility measured at an electric field of 2×10^4 V/cm on heating after p-DTS(FBTTh$_2$)$_2$ recrystallization from the isotropic phase at different cooling rates. Electron mobility in the isotropic phase above 210 °C is independent of cooling rate.

dx.doi.org/10.1021/am505572v | ACS Appl. Mater. Interfaces 2014, 6, 20904−20912

transport in p-DTS(FBTTh$_2$)$_2$ indicates that its LUMO energy level (3.3 eV, ref 10.) is sufficiently deep to avoid chemical instability of anions in the presence of oxygen and water and for the electron trapping on molecular oxygen to obscure the electron transport. It should be noted that since push−pull type semiconductors contain electron-rich and electron-poor moieties in their chemical structures, where HOMO and LUMO orbitals are localized, respectively, the geometrical transport paths for electrons and holes, and therefore characteristics of transport sites, in p-DTS(FBTTh$_2$)$_2$ could significantly differ. For a similar derivative with the dithienosilole (DTS)-benzothiadiazole (BT) unit, the LUMO is localized on BT, whereas the HOMO is shared between DTS and BT.[24]

Below 210 °C, organization of material into an ordered phase of triclinic symmetry, details of which will be discussed below, leads to an over 10-fold increase of hole mobility as compared to the one in the disordered isotropic phase. Interestingly, the behavior of hole mobility below 90 °C differs for cooling rates of 1 °C/min, 10 °C/min or "rapid cooling." The largest hole mobility at room temperature, which is of practical importance, was observed for "rapid cooling" procedure. The highest room temperature mobility of 2×10^{-2} cm^2/(V s) was measured at an electric field of 5×10^3 V/cm (see Discussion of Figure 4a

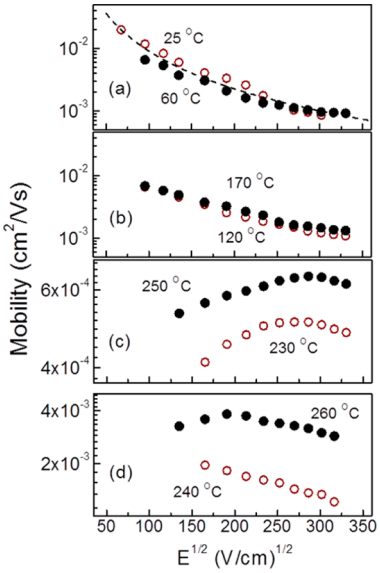

Figure 4. Electric field dependence of (a−c) hole mobility and (d) electron mobility of p-DTS(FBTTh$_2$)$_2$ measured (a, b) in the polycrystalline phases at lower temperatures after rapid crystallization and (c, d) in the isotropic phase at higher temperatures. The dashed line in (a) shows the slope of $\mu \propto E^{-1}$.

below). Surprisingly, slower cooling rates that are expected to lead to a more ordered material, produced smaller mobilities. Note that electron mobility could not be measured at temperatures below 210 °C (Figure 3b) because of the highly dispersive photocurrent transients with no well-defined transit times.

Figure 4 shows the electric field dependence of hole mobility (Figure 4a−c) and electron mobility (Figure 4d) measured at various temperatures that correspond to different structural phases of p-DTS(FBTTh$_2$)$_2$. For isotropic phase, i.e., T > 210 °C, the hole (Figure 4c) and electron (Figure 4d) mobilities initially increase with increasing electric field and then begin to decrease for higher electric fields. The maxima at $E^{1/2} \approx 275$ (V/cm)$^{1/2}$ at 230 °C and at $E^{1/2} \approx 300$ (V/cm)$^{1/2}$ at 250 °C for holes and at $E^{1/2} \approx 200$ (V/cm)$^{1/2}$ at 260 °C for electrons were observed. For lower temperatures, i.e. T < 210 °C (Figures 4a, b), the hole mobility decreases with increasing electric field, i.e. has a negative slope ($d\mu/dE$ < 0). The low temperature behavior of hole mobility is similar to the one in the BHJ of p-DTS(FBTTh$_2$)$_2$ with PC$_{70}$BM at room temperature.[25]

The temperature and electric field dependences of electron and hole mobilities in the isotropic phase at T > 210 °C are typical for uncorrelated hopping over the sites with Gaussian energy distribution and positional disorder.[20] In regard to the temperature dependence, the steady-state charge transport takes place through hopping of charges between the sites around the effective transport energy,[26] whereas charge carriers at deeper energy levels remain trapped and do not contribute to transport (see Scheme S1 in the Supporting Information). As temperature increases, the effective transport energy level moves toward the center of the density of states (DOS) due to the thermal energy available to the charge carriers and, hence, the number of states accessible to the mobile charge carriers increases for the Gaussian density of states. Therefore, mobility increases at higher temperatures. Within this framework, the mobility is described by empirical expression

$$\mu(T, E) = \mu_0 \exp\left[-\left(\frac{2\sigma}{3kT}\right)^2\right] \exp\left\{C\left[\left(\frac{\sigma}{kT}\right)^2 - \Sigma^2\right]E^{1/2}\right\} \quad (1)$$

where μ_0 is the mobility prefactor, i.e., zero-field, infinite temperature value of mobility, σ is the energy width of the hopping site manifold (energetic disorder), Σ is the positional-disorder parameter (for $\Sigma \geq 1.5$), k is the Boltzmann constant, T is the temperature, C is an empirical constant, and E is the electric field strength. From the two-dimensional sets of $\mu(E,T)$ shown in Figures 3a, b and 4c, d, i.e., the temperature and electric field dependences of hole and electron mobility above 210 °C, the values of σ and Σ in the isotropic phase were determined to be 0.11 eV and 2.33, respectively, for hole transport sites and 0.17 eV and 3.55, respectively, for electron transport sites. The higher degree of energy and structural disorder of electron transport sites is consistent with high localization of LUMO on the electron-deficient fluoro-BT unit and, therefore, broader distribution of distances between the electron-transport sites in the disordered state. Alternatively, the activation energies for hole and electron mobilities can be defined, E_A^{hole} = 0.27 eV and E_A^{el} = 0.63 eV, respectively.

The Poole−Frenkel type dependence of mobility on electric field ($\mu \propto SE^{1/2}$, where S is a positive constant) that is observed in the isotropic phase for low electric field (Figure 4c, d) is typical for disordered organic semiconductors. It originates from the fact that the electrostatic energy gain in external electric field reduces the potential barrier for upward hops and makes the charges hop to the sites of larger density of states for the Gaussian energy distribution, therefore increasing the mobility at larger electric fields. The peak formation and negative slope are consistent with the Miller−Abrahams type hopping rate. The downward hops are independent of the energy mismatch between the hoping sites, causing the drift velocity ($v_{drift} = \mu E$) to saturate, therefore producing a mobility that decreases as E^{-1} at larger fields. This is a signature of the material with small energetic disorder, regardless of positional disorder. For the system with energetic and positional disorder, the shift in peak position for different temperatures is mainly

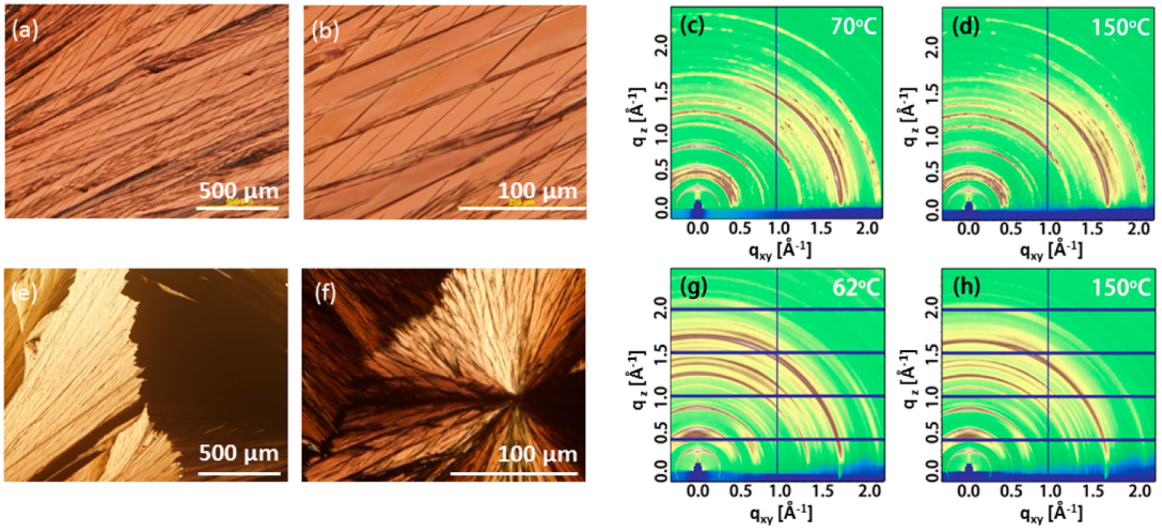

Figure 5. Optical polarized microscopy images of p-DTS(FBTTh$_2$)$_2$ film at 25 °C (a, b) after cooling from the isotropic phase at a rate of 1 °C/min or (e, f) after "rapid cooling". GIXD images of p-DTS(FBTTh$_2$)$_2$ film (c, d) measured on heating after cooling from the isotropic state at a rate of 1 °C/min or (g, h) measured during "rapid cooling".

due to the relative relocation of the effective transport energy level with respect to the center of the density of states (DOS) because of additional thermal energy available to the charge carriers, as described above. According to eq 1, at a given temperature the slope of the field dependence of mobility is governed by the difference between the reduced energetic disorder (σ/kT) and positional disorder Σ. If both contributions are comparable, the dependence of mobility on electric field vanishes, whereas if the positional disorder dominates over the reduced energetic disorder, the mobility decreases with increasing electric field.

The procedure for determining σ and Σ above relies on the assumption that the temperature-induced structural changes are negligible in the isotropic phase. As will be shown below, the ordered phases at lower temperatures are characterized by thermal expansion, therefore requiring to consider temperature-dependent $\sigma(T)$ and $\Sigma(T)$ in the Gaussian disorder formalism. However, for constant σ and Σ at any given temperature (Figure 4a, b), it can be concluded that the negative electric field dependence at lower temperatures is attributed to the small energetic but large positional disorder.[27,28] This phenomenon can be physically visualized for a disordered hopping system with large spatial distribution in terms of faster routes and dead-ends that are created for the carriers executing their random walk. At higher electric fields, the misaligned faster routes with the direction of the external electric field will be diminished; therefore, the carriers will be forced to make the difficult jumps resulting in decreasing mobility with increasing electric field.

Structural Properties. On the basis of DSC measurements (see Figure S1 in the Supporting Information), p-DTS(FBTTh$_2$)$_2$ melts at T_m = 210.78 °C on heating and crystallizes at T_c = 179.47 °C on cooling. Slow cooling of p-DTS(FBTTh$_2$)$_2$ from the molten state produces highly ordered anisotropic structural phases at lower temperatures. Figure 5 compares the polarized optical micrographs of 1 μm thick p-DTS(FBTTh$_2$)$_2$ film at 25 °C after cooling from the isotropic phase, either with a cooling rate of 1 °C/min (Figure 5a, b) or after "rapid cooling" (Figure 5e, f). The slower cooling rate produces significantly larger domains of a parallelogram shape. The identical crystallographic orientation of domains is evident from the uniform color. A characteristic angle of 20°, which reflects the symmetry of a crystallographic unit cell, is observed. The orientation of domains in the rapidly cooled film is more isotropic, as follows from the presence of dark and bright areas in the polarized microscopy images. A significantly smaller size of domains and, therefore, larger number of grain boundaries that can limit the magnitude of mobility are evident too.

Structural order of p-DTS(FBTTh$_2$)$_2$ on molecular scale was examined by the GIXD technique. Shown in Figure 5c, d are the diffraction images of p-DTS(FBTTh$_2$)$_2$ film at 70 and 150 °C, respectively, after slow cooling (1 °C/min). Although the film thickness is quite large, comparable to the thickness of TOF samples, preferred orientation of highly ordered crystallites is clearly visible from the nonuniform azimuthal angular distribution of GIXD features. On the other hand, the angular distribution is more uniform for rapidly cooled film as shown in Figure 5g, h for 62 and 150 °C, respectively.

GIXD scattering profiles at different temperatures are summarized in Figure 6. Panels a and b are the out-of-plane and in-plane line cuts, respectively, for a slow-cooled sample (1 °C/min); panel c is the circular average of scattering for a rapidly cooled sample. The averaging was done because no angular distribution was found. These profiles closely match the diffraction pattern of the same material in the BHJ with P_{70}CBM that was indexed using a single-crystal structure and reported by Nguyen, Bazan and co-workers.[29,30] At room temperature, the p-DTS(FBTTh$_2$)$_2$ forms a triclinic lattice with two molecules per unit cell and lattice parameters: a = 22 Å, b = 3.5 Å, and c = 16 Å. This allows assigning the diffraction peaks as shown in Figures 6a, b. In particular, in slow-cooled films, the $\pi-\pi$ stacking peak at ~1.7 Å^{-1} corresponds to (141) reflection and $\pi-\pi$ stacking distance of 3.5 Å. Stronger intensity of this peak at lower horizontal angles (Figure 6b) in the azimuthal distribution indicates a preferred "edge-on" orientation of molecules with respect to horizontal plane. The (011) diffraction peak at 0.42 Å^{-1} which tracks the end-capping hexyl group spacing of 1.5 nm is significantly larger at low azimuthal angles too. On the other hand, in vertical out-of-plane direction (Figure 6a), the $\pi-\pi$ stacking peak is weak.

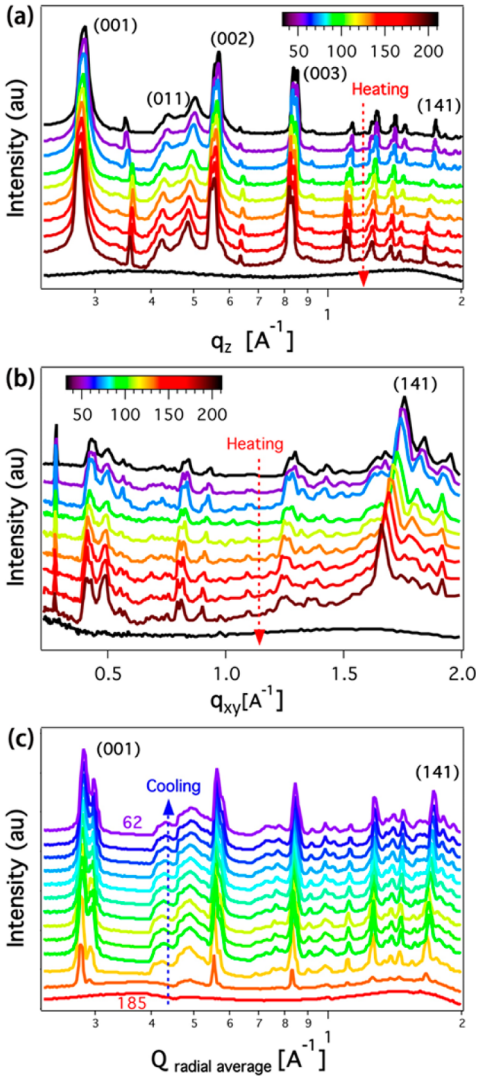

Figure 6. Temperature dependence of GIXD peaks for (a) out-of-plane q_z direction and (b) in-plane q_{xy} direction for p-DTS(FBTTh$_2$)$_2$ film after cooling from isotropic phase at a rate of 1°/min, and (c) temperature dependence of angularly averaged GIXD peaks for p-DTS(FBTTh$_2$)$_2$ film during the melt cooling process.

However, the (001) peak which corresponds to a distance of ~2.2 nm between the branched alkyl groups is very intense, with higher order reflections at 5.8 Å^{-1} (002) and 7.6 Å^{-1} (003) present. This is a dominant orientation in the vertical out-of-plane direction. Therefore, the magnitude of mobility in slowly cooled samples is determined by the transport along the (001) crystallographic orientation, and in particular by the charge transfer across the branched alkyl side groups. An increase of hole mobility in the temperature range from 25 to 90 °C (Figure 3a) indicates that the charge transport is controlled by a large energy disorder of transport sites. The disorder can originate on the molecular scale because of a large intermolecular spacing along the (001) direction or on the mesoscale due to grain boundaries. At the same time, for a rapidly cooled sample (Figure 6c), the diffraction features at the same scattering vectors are observed. However, their uniform azimuthal distribution indicates more isotropic orientation of p-DTS(FBTTh$_2$)$_2$ crystals in such film. In this case, charge transport with higher magnitude of hole mobility (Figure 3a) can occur primarily along the two directions, $\pi-\pi$ stacking and end-capping hexyl group, avoiding the branched alkyl groups direction. The nearly temperature-independent mobility in the range from 25 to 90 °C indicates smaller energy disorder of transport sites in the rapidly cooled film. Note that the in-plane hole mobility of 0.14 cm^2/(V s) was measured in the FET configuration in the films with similar crystallographic orientation, i.e., with dominant (141) peak in the in-plane direction and with (001) and higher order peaks appearing in the out-of-plane direction only.[31] Annealing of such film at 130 °C produces highly ordered, anisotropic film as evidenced by the presence of fifth order (005) diffraction peak and the narrow angular distribution of all the features.[29] Therefore, the observed difference in mobilities for different film processing conditions is a consequence of anisotropic charge transport in sufficiently ordered p-DTS(FBTTh$_2$)$_2$ films. Comparing to the TOF mobility of a rapidly cooled p-DTS(FBTTh$_2$)$_2$ film, hole mobility in the optimized BHJ blends of p-DTS(FBTTh$_2$)$_2$ with PC$_{70}$BM is about an order of magnitude smaller.[25] The difference originates from the fact that the charges in the latter case move along the percolation pathways in the blend whose crystallization kinetics strongly depend on the additive, second component of the blend and processing conditions (solvent, annealing temperature). Such techniques as grazing incidence small-angle X-ray scattering (GISAXS) can be particularly useful for correlating the charge transport properties and morphology of the blends.[32]

To understand the origin of nearly temperature-independent hole mobility in the temperature range between 90 and 210 °C, which is inherent to certain organic semiconductors,[21,33] the temperature dependence of diffraction peak positions shown in Figure 6 for slowly cooled samples was analyzed. Figure 7 shows the lattice expansion of p-DTS(FBTTh$_2$)$_2$ crystals along (001), (141), and (011) crystallographic directions. Table 1 summarizes the linear expansion coefficients. The $\pi-\pi$ stacking

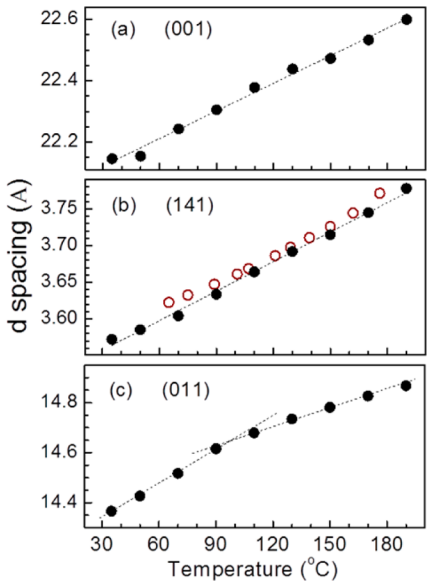

Figure 7. Temperature dependence of *d*-spacing along (a) (001), (b) (141), and (c) (011) crystallographic directions of a triclinic lattice of p-DTS(FBTTh$_2$)$_2$ film. Solid symbols are in situ heating traces and open symbols are melt-cooling traces. Dashed lines show linear fits. (001) and (011) data set is from out-of-plane line-cut profiles; (141) solid symbols are from in-plane cut profiles and open symbols are from radial integrated profiles (reference to Figure 6).

Table 1. Thermal Expansion Coefficients[a]

crystallographic orientation (*hlk*)	prefactor $d^{o}_{(hlk)}$ (Å)	linear expansion coefficient $\alpha_{(hlk)}$ ($\times 10^{-4}$ Å/Å K)
(001) 25 °C < *T* < 210 °C	21.21 ± 0.04	1.41 ± 0.05
(141) 25 °C < *T* < 210 °C	3.15 ± 0.01	4.25 ± 0.15
(011) 25 °C< *T* < 90 °C	14.20 ± 0.01	3.17 ± 0.07
(011) 90 °C < *T* < 210 °C	14.42 ± 0.01	1.60 ± 0.07

[a] $d_{(hlk)} = d^{0}_{(hlk)}(1 + \alpha_{(hlk)}T)$.

direction (141) and branched alkyl-to-alkyl direction (001) are characterized by uniform expansion over the entire temperature range. Since thermal expansion leads to larger intersite distance for charge carrier hoping, which reduces the electron transfer integral,[22] the temperature dependence of hole mobility is a result of competition between thermal activation (positive slope of mobility, $d\mu/dT > 0$) and thermal expansion (negative slope of mobility, $d\mu/dT < 0$). Lattice expansion along (011) direction is nonuniform as follows from the slope change around 90 °C in Figure 7c. This is consistent with the presence of peaks in the temperature-modulated DSC measurements (see Figure S2 in the Supporting Information), indicating a subphase transition. Such temperatures are typical for discotic semiconductors with linear alkyl and alkoxy side chains that undergo phase transition due to melting of side chains. In particular for perylene diimide derivatives, 2D to 3D molecular organization due to registry between the alkyl side chains occurs.[34] Such crystallization leads to formation of grains and introduces strain or cracks at grain boundaries, depending on the degree of contraction. Formation of well-defined grain boundaries in the case of moderate contraction is a probable reason for decreasing mobility and its thermally activated behavior in the slowly cooled samples with dominating (001) orientation along the charge transport direction. This effect is overcompensated by a more isotropic domain orientation, which allows for avoiding unfavorable (001) direction, in the rapidly cooled films.

The extent of $\pi-\pi$ stacking in conjugated solids is another important criterion that determines charge transport properties. This has been analyzed from the area of the (141) reflection to estimate the relative crystallinity of p-DTS$(FBTTh_2)_2$ under the course of thermal treatment in in situ GIXD experiment. Figure 8 shows the temperature dependence of the (141) peak area and provides another evidence for a subphase transition at

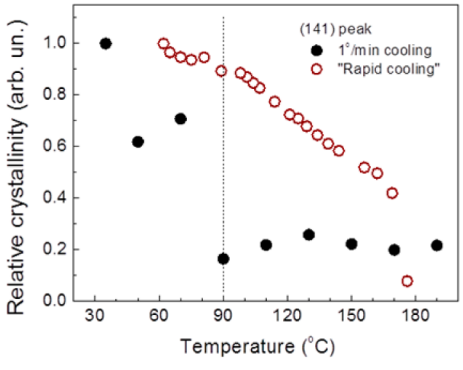

Figure 8. Temperature dependence of (141) peak area for two cooling rates of p-DTS$(FBTTh_2)_2$ normalized at 30 °C.

90 °C. For both rapid cooling and slow heating cycles, a discontinuity of relative crystallinity is seen at this temperature. Rapid cooling arrests long-range motion in a solid which, when coupled with the (141) lattice thermal expansion, indicates that a subphase transition should exist in this temperature region. It is obvious that this phase transition significantly impacts charge transport properties of p-DTS$(FBTTh_2)_2$ films, affecting primarily the mesoscale film morphology.

The described charge carrier transport properties facilitate in explaining some aspects of efficient performance of p-DTS$(FBTTh_2)_2$ as a donor component of the BHJ devices with high power conversion efficiencies up to 9%.[10] First, the ambipolar nature of charge transport should lead to large diffusion length of excitons that are transferred by the Dexter mechanisms since there is no asymmetry in the mobilities of both charge carriers. Not surprisingly, this material works efficiently even with nanodomains size of 30 nm (refs 29 and 35.) which is significantly larger than the typical size of 10 nm in many efficient photovoltaic materials. Second, the hole mobility is the highest reported bulk mobility for photovoltaic materials and well-balanced with electron mobility of $PC_{70}BM$. This helps removing the photogenerated holes faster, decreasing recombination, and prevents an asymmetric charge built-up. Third, the high mobility in isotropic phase indicates that the mobility in the disordered state is also high, therefore charge transport through the disordered regions in the blends can be sufficiently efficient. Finally, thermal annealing of material at temperatures above 90 °C should improve the degree of crystallinity in the domains in the blends with $PC_{70}BM$ molecules because of internal strain relaxation. Sliding of molecules because there is no registry between the side chains is a probably mechanism.

CONCLUSION

The bulk charge carrier transport in push–pull-type organic semiconductor, p-DTS$(FBTTh_2)_2$, was studied in correlation with the structural properties in different structural phases by the time-of-flight and grazing incidence X-ray diffraction techniques. In the disordered isotropic phase, the p-DTS-$(FBTTh_2)_2$ is an ambipolar material with high electron and hole mobilities. Upon phase transition to a polycrystalline film with a triclinic unit-cell symmetry and high degree of anisotropy, a 10-fold increase of hole mobility was observed. The magnitude of mobility is limited by charge propagation along the least efficient crystallographic orientation (001), which corresponds to charge transfer across the branched alkyl side chains. The temperature independence of mobility within this phase is consistent with thermal expansion. Surprisingly, despite the fact that faster cooling rates result in more disordered morphology at temperatures below 90 °C, more isotropic orientation of domains produces even large hole mobilities in this case. A hole mobility as high as 2×10^{-2} $cm^2/(V\ s)$ at an electric field of 5×10^3 V/cm could be achieved at 25 °C. Implications of these results for material processing and performance as a donor component in the BHJ photovoltaic devices were discussed.

ASSOCIATED CONTENT

Supporting Information

DSC and temperature-modulated DSC scans, typical photocurrent transients in double logarithmic scales representation, polarized optical micrographs of 11 μm thick films, and a scheme of energy relaxation of photoexcited charge carriers

during the elementary hopping steps in a disordered semiconductor. This material is available free of charge via the Internet at http://pubs.acs.org.

AUTHOR INFORMATION

Corresponding Authors

*E-mail: duzhko@mail.pse.umass.edu.

* E-mail: russell@mail.pse.umass.edu.

Present Address

[†]F.L. is currently at Lawrence Berkley National Laboratory, Berkley, CA.

Author Contributions

The manuscript was written through contributions of all authors. All authors have given approval to the final version of the manuscript.

Notes

The authors declare no competing financial interest.

ACKNOWLEDGMENTS

This work was supported as part of Polymer-Based Materials for Harvesting Solar Energy, an Energy Frontier Research Center funded by the U.S. Department of Energy, Office of Science, Office of Basic Energy Sciences, under Award DE-SC0001087. The GIXD part was carried out at and supported by the Advance Light Source, Lawrence Berkeley National Laboratory, supported by the U.S. Department of Energy, Office of Science, Office of Basic Energy Sciences.

ABBREVIATIONS

p-DTS(FBTTh$_2$)$_2$, 7,7′-(4,4-bis(2-ethylhexyl)-4H-silolo[3,2-b:4,5-b′]dithiophene-2,6-diyl)bis(6-fluoro-4-(5′-hexyl-[2,2′-bithiophen]-5yl)benzo[c][1,2,5]thiadiazole)

TOF, time-of-flight

GIXD, grazing incidence X-ray diffraction

OPV, organic photovoltaic device

FET, field-effect transistor

DSC, differential scanning calorimetry

REFERENCES

(1) Heeger, A. J. 25th Anniversary Article: Bulk Heterojunction Solar Cells: Understanding the Mechanism of Operation. *Adv. Mater.* **2014**, *26*, 10−28.

(2) Dou, L.; You, J.; Hong, Z.; Xu, Z.; Li, G.; Street, R. A.; Yang, Y. 25th Anniversary Article: A Decade of Organic/Polymeric Photovoltaic Research. *Adv. Mater.* **2013**, *25*, 6642−6671.

(3) Zulkarnaen, S.; Piliego, C.; Gao, J.; Loi, M. A. Outlook and Emerging Semiconducting Materials for Ambipolar Transistors. *Adv. Mater.* **2014**, *26*, 1176−1199.

(4) van Mullekom, H. A. M.; Vekemans, J. A. J. M.; Havinga, E. E.; Meijer, E. W. Developments in the Chemistry and Band Gap Engineering of Donor-Acceptor Substituted Conjugated Polymers. *Mater. Sci. Eng.* **2001**, *32*, 1−40.

(5) Beaujuge, P. M.; Frechet, J. M. J. Molecular Design and Ordering Effects in π-Functional Materials for Transistor and Solar Cell Applications. *J. Am. Chem. Soc.* **2011**, *133*, 20009−20029.

(6) Boudreault, P.-L. T.; Najari, A.; Leclerc, M. Processable Low-Bandgap Polymers for Photovoltaic Applications. *Chem. Mater.* **2011**, *23*, 456−469.

(7) Li, J.; Zhao, Y.; Tan, H. S.; Guo, Y.; Di, C.-A.; Yu, G.; Liu, Y.; Lin, M.; Lim, S. H.; Zhou, Y.; Su, H.; Ong, B. S. A Stable Solution-Processed Polymer Semiconductor with Record High-Mobility for Printed Transistors. *Sci. Rep.* **2012**, *2*, 754.

(8) Zhang, X.; Bronstein, H.; Kronemeijer, A. J.; Smith, J.; Kim, Y.; Kline, R. J.; Richter, L. J.; Anthopoulos, T. D.; Sirringhaus, H.; Song, K.; Heeney, M.; Zhang, W.; McCulloch, I.; Delongchamp, D. Molecular Origin of High Field-Effect Mobility in an Indacenodithiophene−benzothiadiazole Copolymer. *Nat. Commun.* **2013**, *4*, 2238.

(9) He, Z.; Zhong, C.; Su, S.; Xu, M.; Wu, H.; Cao, Y. Enhanced Power-Conversion Efficiency in Polymer Solar Cells Using an Inverted Device Structure. *Nat. Photonics* **2012**, *6*, 591.

(10) Kyaw, A. K. K.; Wang, D. H.; Wynands, D.; Zhang, J.; Nguyen, T. Q.; Bazan, G. C.; Heeger, A. J. Improved Light Harvesting and Improved Efficiency by Insertion of an Optical Spacer (ZnO) in Solution-Processed Small-Molecule Solar Cells. *Nano Lett.* **2013**, *13*, 3796−3801.

(11) Proctor, C. M.; Love, J. A.; Nguyen, T.-Q. Mobility Guidelines for High Fill Factor Solution-Processed Small Molecule Solar Cells. *Adv. Mater.* **2014**, DOI: 10.1002/adma.201401725.

(12) Sirringhaus, H.; Brown, P. J.; Friend, R. H.; Nielsen, M. M.; Bechgaard, K.; Langeveld-Voss, B. M. W.; Spiering, A. J. H.; Janssen, R. A. J.; Meijer, E. W.; Herwig, P.; de Leeuw, D. M. Two-dimensional Charge Transport in Self-organized, High-Mobility Conjugated Polymers. *Nature* **1999**, *401*, 685−688.

(13) Takacs, C. J.; Treat, N. D.; Kramer, S.; Chen, Z.; Facchetti, A.; Chabinyc, M. L.; Heeger, A. J. Remarkable Order of a High-Performance Polymer. *Nano Lett.* **2013**, *13*, 2522−2527.

(14) Kronemeijer, A. J.; Pecunia, V.; Venkateshvaran, D.; Nikolka, M.; Sadhanala, A.; Moriarty, J.; Szumilo, M.; Sirringhaus, H. Two-Dimensional Carrier Distribution in Top-Gate Polymer Field-Effect Transistors: Correlation between Width of Density of Localized States and Urbach Energy. *Adv. Mater.* **2014**, *26*, 728−733.

(15) Spear, W. E. Drift Mobility Technique for the Study of Electrical Transport Properties in Insulating Solids. *J. Non-Cryst. Solids* **1969**, *1*, 197−214.

(16) Lebedev, E.; Dittrich, Th.; Petrova-Koch, V.; Karg, S.; Bruetting, W. Charge Carrier Mobility in Poly(p-phenylenevinylene) Studied by the Time-of-flight Technique. *Appl. Phys. Lett.* **1997**, *71*, 2686−2688.

(17) Shen, X.; Duzhko, V. V.; Russell, T. P. Study on the Correlation Between Structure and Hole Transport in Semi-Crystalline Regioregular P3HT. *Adv. Energy Mater.* **2013**, *3*, 263−270.

(18) Gupta, V.; Kyaw, A. K. K.; Wang, D. H.; Chand, S.; Bazan, G. C.; Heeger, A. J. Barium: An Efficient Cathode Layer for Bulk-heterojunction Solar Cells. *Sci. Rep.* **2013**, *3*, 1965.

(19) Photovoltaic device with regular (non-inverted) device architecture produced power conversion efficiencies of 7.0 ± 0.2% in our laboratory, consistent with previous publications by other groups and indicating comparable material purity. Karak, S.; Page, Z. A.; Emrick, T.; Duzhko, V. V. Raising Efficiency of Organic Solar Cells with Electrotropic Additives. *Appl. Phys. Lett.* **2014**, submitted.

(20) Bässler, H. Charge Transport in Disordered Organic Photoconductors. A Monte Carlo Simulation Study. *Phys. Status Solidi B* **1993**, *175*, 15−56.

(21) Duzhko, V.; Aqad, E.; Imam, M. R.; Peterca, M.; Percec, V.; Singer, K. D. Long-range Electron Transport in a Self-Organizing N-type Organic Material. *Appl. Phys. Lett.* **2008**, *92*, 113312.

(22) Coropceanu, V.; Cornil, J.; da Silva Filho, D. A.; Olivier, Y.; Silbey, R.; Bredas, J.-L. Charge Transport in Organic Semiconductors. *Chem. Rev.* **2007**, *107*, 926−952.

(23) Zaumseil, J.; Sirringhaus, H. Electron and Ambipolar Transport in Organic Field-Effect Transistors. *Chem. Rev.* **2007**, *107*, 1296−1323.

(24) Chen, H.-Y.; Hou, J.; Hayden, A. E.; Yang, H.; Houk, K. N.; Yang, Y. Silicon Atom Substitution Enhances Interchain Packing in a Thiophene-Based Polymer System. *Adv. Mater.* **2010**, *22*, 371−375.

(25) Proctor, C. M.; Albrecht, S.; Kuik, M.; Neher, D.; Nguyen, T.-Q. Overcoming Geminate Recombination and Enhancing Extraction in Solution-Processed Small Molecule Solar Cells. *Adv. Energy Mater.* **2014**, 1400230.

(26) Deibel, C.; Dyakonov, V. Polymer−Fullerene Bulk Heterojunction Solar Cells. *Rep. Prog. Phys.* **2010**, *73*, 096401.

(27) Mozer, A. J.; Sariciftci, N. S. Negative Electric Field Dependence of Charge Carrier Drift Mobility in Conjugated, Semiconducting Polymers. *Chem. Phys. Lett.* **2004**, *389*, 438−442.

(28) Mozer, A. J.; Sariciftci, N. S.; Pivrikas, A.; Österbacka, R.; Juška, G.; Brassat, L.; Bässler, H. Charge Carrier Mobility in Regioregular Poly(3-hexylthiophene) Probed by Transient Conductivity Techniques: A Comparative Study. *Phys. Rev. B* **2005**, *71*, 035214.
(29) Love, J. A.; Proctor, C. M.; Liu, J.; Takacs, C. J.; Sharenko, A.; van der Poll, T. S.; Heeger, A. J.; Bazan, G. C.; Nguyen, T.-Q. Film Morphology of High Efficiency Solution-Processed Small-Molecule Solar Cells. *Adv. Funct. Mater.* **2013**, *23*, 5019−5026.
(30) Perez, L. A.; Chou, K. W.; Love, J. A.; van der Poll, T. S.; Smilgies, D. M.; Nguyen, T.-Q.; Kramer, E. J.; Amassian, A.; Bazan, G. C. Solvent Additive Effects on Small Molecule Crystallization in Bulk Heterojunction Solar Cells Probed During Spin Casting. *Adv. Mater.* **2013**, *25*, 6380−6384.
(31) Kyaw, A. K. K.; Wang, D. H.; Gupta, V.; Leong, W. L.; Ke, L.; Bazan, G. C.; Heeger, A. J. Intensity Dependence of Current Voltage Characteristics and Recombination in High-Efficiency Solution-Processed Small-Molecule Solar Cells. *ACS Nano* **2013**, *7*, 4569−4577.
(32) Müller-Buschbaum, P. The Active Layer Morphology of Organic Solar Cells Probed with Grazing Incidence Scattering Techniques. *Adv. Mater.* **2014**, DOI: 10.1002/adma.201304187.
(33) Iino, H.; Hanna, J.-i.; Bushby, R. J.; Movaghar, B.; Whitaker, B. J.; Cook, M. J. Very High Time-of-flight Mobility in the Columnar Phases of a Discotic Liquid Crystal. *Appl. Phys. Lett.* **2005**, *87*, 132102.
(34) Percec, V.; Peterca, M.; Tadjiev, T.; Zeng, X.; Ungar, G.; Leowanawat, P.; Aqad, E.; Imam, M. I.; Rosen, B. M.; Akbey, U.; Graf, R.; Sekharan, S.; Sebastini, D.; Spiess, H. W.; Heiney, P. A.; Hudson, S. D. Self-Assembly of Dendronized Perylene Bisimides into Complex Helical Columns. *J. Am. Chem. Soc.* **2011**, *133*, 12197−12219.
(35) Gelinas, S.; Rao, A.; Kumar, A.; Smith, S. L.; Chin, A. W.; Clark, J.; van der Poll, T. S.; Bazan, G. C.; Friend, R. H. Ultrafast Long-Range Charge Separation in Organic Semiconductor Photovoltaic Diodes. *Science* **2014**, *343*, 512−516.